Microsc. Microanal. 14, 16–26, 2008
DOI: 10.1017/S1431927608080045

Microscopy AND Microanalysis

Contrast Transfer and Resolution Limits for Sub-Angstrom High-Resolution Transmission Electron Microscopy

Markus Lentzen*

Institute of Solid State Research, Ernst Ruska Centre for Microscopy and Spectroscopy with Electrons, Research Centre Jülich, 52425 Jülich, Germany

Abstract: The optimum imaging of an object structure at the sub-angstrom length scale requires precise adjustment of the lens aberrations of a high-resolution instrument up to the fifth order. A least-squares optimization of defocus aberration C_1, third-order spherical aberration C_3, and fifth-order spherical aberration C_5 yields two sets of aberration coefficients for strong phase contrast up to the information limit: one for variable C_1 and C_3, at fixed C_5, another for variable C_1, C_3, and C_5. An additional correction to the defocus aberration, dependent on object thickness, is described, which becomes important for the use of image simulation programs in predicting optimum high-resolution contrast from thin objects at the sub-angstrom scale. For instruments with a sub-angstrom information limit the ultimate structure resolution, the power to resolve adjacent atom columns in a crystalline object, depends on both the instrumental pointspread and an object pointspread due to finite width of the atomic column potentials. A simulation study on a simple double-column model yields a range for structure resolutions, dependent on the atomic scattering power, from 0.070 nm down to 0.059 nm, for a hypothetical 300-kV instrument with an information limit of 0.050 nm.

Key words: high-resolution electron microscopy, aberration correction, contrast theory, optimum imaging, resolution limit

Introduction

In the past years the information limit of midvoltage high-resolution transmission electron microscopy has been extended notably toward the sub-angstrom scale. The deleterious effect of chromatic aberration, which sets the limit upon instrumental resolution today, has been reduced by the use of field-emission sources combined with more stable lens and high-voltage power supplies (Lichte, 1986; Kisielowski et al., 2001; O'Keefe et al., 2001). Recently, information limits have been further improved through the use of gun monochromators, which reduce the energy spread of the illuminating electron wave substantially (Benner et al., 2003; Freitag et al., 2005).

The interpretability of structure images, which is equally important as an improved information limit, has been improved as well through lens-aberration measurement and correction. Hardware aberration correction strongly reduces the unwanted delocalization of contrast details in the image plane (Rose, 1990; Haider et al., 1998), induced not only by the large spherical aberration of the objective lens but also by other residual aberrations of the imaging system such as twofold astigmatism, second-order coma, and threefold astigmatism, to name but a few. Software aberration correction acting upon the experimentally retrieved exit wave function in the image plane virtually eliminates unwanted delocalization, down to the limit given by measurement errors (Lichte, 1991; Coene et al., 1992; Thust et al., 1996).

Hardware aberration correctors can be used to optimize the structure image of a thin object by tuning defocus and third-order spherical aberration in order to extend the Scherzer passband (Scherzer, 1949) just beyond the information limit. Under these conditions phase contrast is established over a wide range of spatial frequencies in combination with a low delocalization in the image plane (Lentzen et al., 2002). If further the lens aberration function is chosen positive, that is, the lens is set to overfocus combined with negative spherical aberration, then the resulting negative phase contrast yields enhanced bright-atom contrast in the image plane (Rose, 1989; Jia et al., 2004), which may be favorably exploited to detect even light-atom columns close to heavy-atom columns (Jia et al., 2003; Jia & Urban, 2004).

At sub-angstrom resolution the phase shift by the fifth-order spherical aberration of today's objective lenses starts to play a role for the transfer of highest spatial frequencies. Scherzer proposed for the optimum imaging of a thin object the use of special defocus and third-order spherical

Received October 17, 2006; Accepted August 2, 2007.
*E-mail: m.lentzen@fz-juelich.de

aberration values, if contrast transfer is limited by fifth-order spherical aberration alone (Scherzer, 1949, 1970). Chang et al. (2006) extended the treatment to a variable fifth-order spherical aberration that was adapted to shift the first zero of the contrast transfer function to the information limit.

In this work two alternative sets of conditions for the optimum imaging of thin objects are derived by adapting an optimum phase plate over the virtual aperture given by the temporal coherence envelope. The first set gives defocus and third-order spherical aberration as a function of wavelength and information limit for a fixed fifth-order spherical aberration; the second set gives defocus, third-order spherical aberration, and fifth-order spherical aberration as a function of wavelength and information limit if the hardware aberration corrector allows tuning of the fifth-order spherical aberration. For both sets a favorable phase shift of $\pm\pi/2$ of the scattered electron wave is established over a broad passband.

Further, a correction of the defocus values entered in standard image simulation programs is discussed, which relates to the different conventional choices of the reference plane for zero defocus in experiment and simulation. The defocus correction becomes important if simulation programs are used for the prediction of sub-angstrom high-resolution contrast from thin objects.

Any of the above optimum aberration settings seeks to yield a narrow peak of the pointspread function of the instrument, yet there are deficiencies: small spatial frequencies are transmitted poorly, and the desire for phase contrast introduces via the gradient of the aberration function an unwanted residual delocalization. The residual blur in the image plane due to both effects deserves attention with respect to sub-angstrom contrast transfer.

The interpretability of the final structure image of crystalline objects with respect to intercolumn distances, its "structure resolution," is not determined only by the pointspread of the instrument. As the atomic electrostatic potentials, and hence also projected atom-column potentials, have finite width, one cannot, in principle, expect with improving instrumental resolution an ever-growing structure resolution (Van Dyck & de Jong, 1992; Van Dyck et al., 1992, 2004; O'Keefe et al., 2005). To a certain degree the object itself carries a pointspread that deserves, as well, attention with respect to sub-angstrom contrast transfer.

In the last part of this work estimates are given for the pointspread due to the width of projected column potentials and the pointspread introduced by electron scattering, each for a range of atom columns with different scattering powers. The resulting object pointspreads are compared with the optimum instrumental pointspread and the contrast width of the related image intensity. The structure resolution, which is the important value for practical work, is then determined from the spacing of two adjacent columns that can be just resolved according to the Rayleigh criterion.

Optimum Contrast Transfer Functions

In transmission electron microscopy the image contrast from a weak-phase object can be enhanced by the use of a proper phase shift induced by the imaging system. Scherzer adopted Zernike's method of phase contrast in light microscopy (Zernike, 1942*a*, 1942*b*, 1955) and derived expressions for objective lens defocus, third-order spherical aberration, and fifth-order spherical aberration, which impose on the scattered electron wave an additional phase shift (Scherzer, 1970). For fixed positive third-order spherical aberration and an optimum underfocus, the additional phase shift adopts a value of $+\pi/2$ over a broad passband, and at that positive phase-contrast condition atoms appear dark relative to the mean intensity. For fixed positive fifth-order spherical aberration, the optimum third-order spherical aberration is negative, the optimum defocus is positive, that is, at overfocus, and the additional phase shift adopts a value of $-\pi/2$ over a broad passband. At that negative phase-contrast condition atoms appear bright relative to the mean intensity.

Scherzer used two conditions in the derivation of the two sets of optimum aberrations: first, maintaining a favorable phase shift of $\pm\pi/2$ over a passband as broad as possible, second, shifting the first zero of the contrast transfer function to a spatial frequency as large as possible. The derivation comprises an optimization over one dimension of spatial frequencies, a method used in later work as well (O'Keefe, 2000; Lentzen et al., 2002; Chang et al., 2006).

Alternatively, the optimization of the contrast transfer function can be carried out in the two-dimensional space of spatial frequencies with coordinates (g_1, g_2), which appears to be a more natural choice, as the phase shift induced by the imaging system is described by the two-dimensional aberration function $\chi(g_1, g_2)$. In a footnote of Scherzer (1970) and by Scherzer and Typke (1967) this alternative is mentioned and used in order to determine an average pointspread in the presence of noncircular-symmetric aberrations.

In the following treatment we adopt Scherzer's proposal of a two-dimensional treatment of the optimization problem, as in Lentzen (2004), and we consider now the first three circular-symmetric aberrations: defocus C_1, third-order spherical aberration C_3, and fifth-order spherical aberration C_5. The phase shift $-2\pi\chi(g_1, g_2)$ induced by the imaging system, with the aberration function

$$\chi(g_1, g_2) = \frac{1}{2} C_1 \lambda (g_1^2 + g_2^2) + \frac{1}{4} C_3 \lambda^3 (g_1^2 + g_2^2)^2 + \frac{1}{6} C_5 \lambda^5 (g_1^2 + g_2^2)^3, \quad (1)$$

should adopt a value of $-\pi/2$ over the circular region in reciprocal space given by the virtual aperture A, radius $g_{\max}$, due to the temporal coherence envelope. With this phase shift, the imaging system transmits the scattered electron wave with negative phase contrast.

The least-squares fit

$$\iint_A \left| \chi(g_1, g_2) - \frac{1}{4} \right|^2 dg_1\, dg_2 = 2\pi \int_0^{g_{\max}} \left| \chi(g) - \frac{1}{4} \right|^2 g\, dg \to \min. \tag{2}$$

of the aberration function (1) to the optimum value $\chi = \frac{1}{4}$ yields two sets of optimum aberration coefficients: one for fixed fifth-order spherical aberration C_5, namely,

$$C_1 = \frac{2}{\lambda g_{\max}^2} + \frac{2}{15} C_5 \lambda^4 g_{\max}^4, \tag{3a}$$

$$C_3 = -\frac{10}{3\lambda^3 g_{\max}^4} - \frac{8}{9} C_5 \lambda^2 g_{\max}^2, \tag{3b}$$

and another for variable fifth-order spherical aberration C_5, namely,

$$C_1 = \frac{15}{4\lambda g_{\max}^2}, \tag{4a}$$

$$C_3 = -\frac{15}{\lambda^3 g_{\max}^4}, \tag{4b}$$

$$C_5 = \frac{105}{8\lambda^5 g_{\max}^6}, \tag{4c}$$

with the information limit $g_{\max}$ and the electron wavelength λ.

All coefficients change sign, if positive phase contrast is desired, where atoms appear dark relative to the mean image intensity. For $C_5 = 0$ mm the set of aberration coefficients (3) reduces to the values given by Lentzen (2004), where Scherzer's proposal of a two-dimensional treatment of the optimization problem had already been used.

The action of the two optimum sets of aberrations (3) and (4) on contrast transfer is elucidated by drawing the lens aberration function $\chi(g)$ and the contrast transfer function $\sin 2\pi\chi(g)$ for three cases: (1) a microscope with a fixed, corrected fifth-order spherical aberration $C_5 = 0$ mm; (2) a microscope with a fixed, uncorrected fifth-order spherical aberration of $C_5 = 4$ mm, which is a typical value for a modern objective lens; (3) a microscope with a variable fifth-order spherical aberration. For all three cases the coherent part of the linear contrast transfer function was considered; the envelope functions due to spatial and temporal coherence were left aside for a clearer view of the phase changes induced at the highest spatial frequencies.

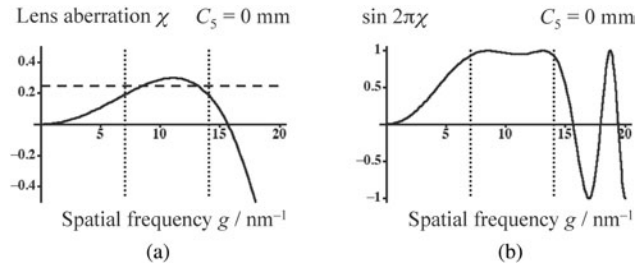

Figure 1. Contrast transfer for $C_1 = 4.9$ nm, $C_3 = -10$ μm, and $C_5 = 0$ mm. **a:** Lens aberration function χ. **b:** Contrast transfer function $\sin 2\pi\chi$, envelopes due to partial coherence left aside. Dotted lines denote the upper and lower bounds of the Scherzer $\pi/2$ passband. The broken line denotes the aberration $\chi = \frac{1}{4}$, favorable for the imaging of weak phase objects.

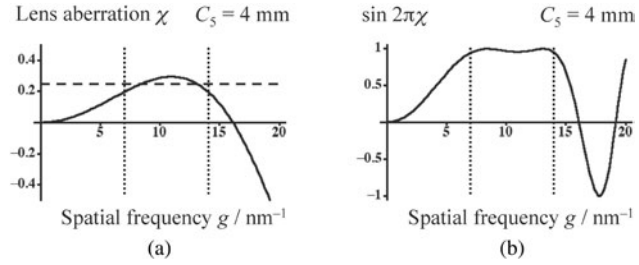

Figure 2. Contrast transfer for $C_1 = 5.3$ nm, $C_3 = -13$ μm, and $C_5 = 4$ mm. **a:** Lens aberration function χ. **b:** Contrast transfer function $\sin 2\pi\chi$, envelopes due to partial coherence left aside. Dotted lines denote the upper and lower bounds of the Scherzer $\pi/2$ passband. The broken line denotes the aberration $\chi = \frac{1}{4}$, favorable for the imaging of weak phase objects.

For an accelerating voltage of 300 kV and an information limit of $g_{\max} = 1/0.07$ nm^{-1} the C_5-corrected instrument has optimum contrast transfer for $C_1 = 4.9$ nm and $C_3 = -10$ μm. The lens aberration function and the contrast transfer function are displayed in Figure 1, together with upper and lower bounds of the Scherzer passband.

The microscope with a fixed, uncorrected fifth-order spherical aberration of $C_5 = 4$ mm has optimum contrast transfer for $C_1 = 5.3$ nm and $C_3 = -13$ μm. The lens aberration function and the contrast transfer function are displayed in Figure 2, together with upper and lower bound of the Scherzer passband. Compared to the C_5 corrected instrument, the defocus C_1 is slightly larger, and the third-order spherical aberration C_3 has a slightly larger negative value. The contrast transfer, however, is identical up to the information limit, and the oscillations of the contrast transfer function beyond the information limit are slightly slower. Hence, a value of C_5 in the order of a few millimeters has no

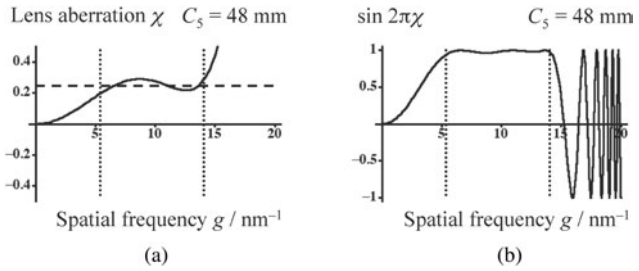

Figure 3. Contrast transfer for $C_1 = 9.2$ nm, $C_3 = -45$ μm, and $C_5 = 48$ mm. **a:** Lens aberration function χ. **b:** Contrast transfer function $\sin 2\pi\chi$, envelopes due to partial coherence left aside. Dotted lines denote the upper and lower bounds of the Scherzer $\pi/2$ passband. The broken line denotes the aberration $\chi = \frac{1}{4}$, favorable for the imaging of weak phase objects.

effect on the contrast transfer at an accelerating voltage of 300 kV and an information limit of 1/0.07 nm^{-1}.

The microscope with a variable fifth-order spherical aberration has optimum contrast transfer for $C_1 = 9.2$ nm, $C_3 = -45$ μm, and $C_5 = 48$ mm. The lens aberration function and the contrast transfer function are displayed in Figure 3, together with upper and lower bounds of the Scherzer passband. Compared to the two microscpes considered above, with small or zero fifth-order spherical aberration, the defocus C_1 has almost doubled, and the third-order spherical aberration C_3 has a more than three times larger negative value. The very large value of C_5 is out of reach for today's aberration correctors, but may be adjustable in future electron-optical layouts (M. Haider, personal communication, 2005). Contrast transfer is improved considerably over that for microscopes with small fifth-order spherical aberration: the lower bound of the Scherzer passband extends to spatial frequencies smaller than 5 nm^{-1} and is thus enhanced by about 2 nm^{-1}. Strong oscillations of the contrast transfer function appear only beyond the information limit and hence do not disturb high-resolution imaging.

The lens aberration functions displayed in Figures 1, 2, and 3 reveal another benefit of the two-dimensional least-squares fit (2): the Scherzer phase plate maintains a favorable value of $\chi \approx \frac{1}{4}$ up to the information limit, and large gradients, which give rise to a displacement

$$\vec{R}(\vec{g}) = \frac{\partial \chi}{\partial \vec{g}} \tag{5}$$

of a ray with spatial frequency $\vec{g}$ in the image plane, appear only for spatial frequencies beyond the information limit. Hence the method used in this work gives aberration coefficients for optimum phase plates with reduced delocalization.

The delocalization of the optimum aberration functions defined by the sets of coefficients (3) and (4) is defined by the largest displacement R in the image plane for any ray inside the virtual aperture A (Lichte, 1991; Coene & Jansen, 1992):

$$R = \max_{\vec{g}\,\text{in}\,A} |\vec{R}(\vec{g})|. \tag{6}$$

For the optimum aberrations (4) including a variable fifth-order spherical aberration the delocalization is $R = \frac{15}{8} g_{\max}^{-1}$.

Defocus Correction for Image Simulation

Objects used for high-resolution investigations often have thicknesses smaller than ~10 nm. At those thicknesses, less than half the extinction distance of different column species of a crystalline material, the phase shift of the scattered electron wave is related to the scattering power of distinct columns: columns of low nuclear charge per column length impose a small phase shift; columns of high nuclear charge per column length impose a strong phase shift (Kambe et al., 1974; Fujimoto, 1978). Further, at small object thickness, the asymmetry of contrast features due to object tilt with respect to the illuminating electron wave are less pronounced (Smith et al., 1983).

For sub-angstrom resolution the different optimum defoci of the imaging system (O'Keefe, 2000; Lentzen et al., 2002; Lentzen, 2004; Chang et al., 2006) approach values less than ~10 nm as well. Object thickness and defocus then have comparable values, and it is therefore worthwhile to determine the exact location of the optimum focus plane with respect to the object.

In image simulation programs the Gaussian image plane, the plane of zero defocus, is placed at the exit face of the object, because the chiefly used methods for the calculation of electron scattering, the Bloch wave formalism (Bethe, 1928) and the multislice algorithm (Cowley & Moodie, 1957), yield as a result the scattered electron wave at the exit face.

Whether or not this choice is appropriate for sub-angstrom high-resolution imaging can be assessed by invoking the kinematical approximation of electron scattering. For crystalline objects distinctly thinner than half the extinction distance of the most strongly scattering column, the amplitude of the transmitted beam is still close to 1. Then the kinematical integration of the scattered partial waves, excluding multiple scattering, is a good approximation to the result of the full multislice iteration, which includes multiple scattering.

The kinematical integration yields for a scattered ray with spatial frequency $\vec{g}$

$$\begin{aligned}\psi(\vec{g}, t) &= \int_0^t \pi i \lambda U(\vec{g}, t') e^{-\pi i \lambda g^2 t'}\, dt' \\ &= \pi i \lambda U(\vec{g})\, \frac{\sin \frac{1}{2}\pi\lambda g^2 t}{\frac{1}{2}\pi\lambda g^2}\, e^{-(1/2)\pi i \lambda g^2 t},\end{aligned} \tag{7}$$

with object thickness t, crystal potential $U(\vec{g}, t')$, and its average $U(\vec{g})$ over the object thickness. The complex amplitude of the scattered electron wave (7) is proportional to the projected crystal potential, includes the kinematical damping envelope, and a phasor representing a defocus aberration equal to half the object thickness. This overfocus of $t/2$ induces a delocalization of $\frac{1}{2}t\lambda\vec{g}$ of the scattered ray $\vec{g}$ in the exit plane, which adds to the delocalization (5) through the imaging system of the microscope.

If the scattered electron wave (7) is now refocused by a defocus of $-t/2$, that is, an underfocus toward the midplane of the object,

$$\psi_{\text{corr}}(\vec{g}, t) = \psi(\vec{g}, t)e^{(1/2)\pi i\lambda g^2 t}, \tag{8}$$

then the phasor in (7) and its delocalization are compensated, and $\psi_{\text{corr}}(\vec{g}, t)$ would result in a more faithful image of the projected crystal potential $U(\vec{g})$ in the image plane of the microscope. The refocusing of the exit plane wave function is intuitively executed by a microscope operator seeking to record a "sharp" image, near Scherzer defocus, of the thin object under investigation, but in image simulation programs, such automatic refocusing toward the optimum plane for structure imaging is not performed and has to be considered at input of the defocus value used for simulation.

For thick amorphous objects, with thicknesses as large as 100 nm, Bonhomme and Beorchia (1983) described the respective systematical error in defocus measurements using Thon rings, if the reference plane for the measurement, that is, the Gaussian image plane, is assumed to be the exit plane and not the midplane of the object.

For thin amorphous objects or thin crystalline objects the required change of defocus for phase contrast with specimen thickness was deduced in past years from simulated image contrast maps over defocus and specimen thickness (see, e.g., the work of O'Keefe et al., 1989). The refocusing by $t/2$, however, was not important, because, at the information limits of worse than ~0.14 nm of the high-resolution instruments then used and Scherzer defoci of around −50 nm, a defocus change of ~5 nm has almost no effect on contrast transfer. Now, for information limits of 0.1 nm and better, in combination with the small optimum defoci of <10 nm used in aberration-corrected instruments, the same refocusing has strong impact on structure imaging.

The effect of refocusing by half the specimen thickness (8) is elucidated by drawing the intensity profile across two closely spaced Si columns, comprising 5 atoms each, for an accelerating voltage of 300 kV and an information limit of $g_{\max} = 1/0.05\ \text{nm}^{-1}$. The intercolumn distance is 0.064 nm, and the column length $t = 2$ nm. Figure 4 displays two intensity profiles, both simulated for optimum defocus $C_1 = 2.2$ nm and optimum spherical aberration $C_3 = -1.85\ \mu$m (3), assuming $C_5 = 0$ mm. For the lens defocus $Z = C_1 - t/2 = 1.2$ nm, including the underfocus $-t/2$ toward the midplane of the object, the intensity profile displayed in Figure 4a yields two distinct peaks, that is, the closely spaced Si columns are resolved according to the Rayleigh criterion. For lens defocus $Z = C_1$ the intensity profile displayed in Figure 4b yields a broad peak between the column positions, that is, the closely spaced Si columns are not resolved. Comparison of both intensity profiles shows that the small defocus correction (8) helps to provide a more faithful image of the projected column structure.

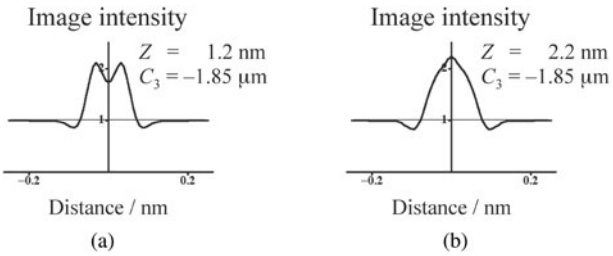

Figure 4. Image intensity of two Si columns comprising 5 atoms each, for an accelerating voltage of 300 kV and an information limit of 0.5 Å. The intercolumn distance is 0.64 Å, and the column length is 2 nm. **a:** Lens defocus of +1.2 nm, third-order spherical aberration of −1.85 μm. **b:** Lens defocus of +2.2 nm, third-order spherical aberration of −1.85 μm.

Resolution Limits for Structure Imaging

The interpretability of a high-resolution structure image with respect to the true object structure is largely determined by the information limit of the instrument, the width of the favorable passband for positive or negative phase contrast, and the delocalization in the image plane. Any choice for an optimum contrast transfer of the instrument is, however, a compromise between the amount of phase contrast and the amount of delocalization, which are both linked via the aberration function (1) and its gradient (5). The resulting instrumental pointspread function can be assessed for a given model object structure with the help of image simulation programs, for example, EMS (Stadelmann, 1987) or MacTempas (O'Keefe & Kilaas, 1988).

To reveal the very detail of object structures, the information limit, the width of the passband for phase contrast, and the delocalization in the image plane have been improved in the past decade toward the sub-angstrom range. The "structure resolution," the power to resolve, for example, adjacent atom columns of a crystalline specimen, improved toward the sub-angstrom range as well.

The limit of structure resolution is, however, not given by the instrumental resolution alone: the atomic electrostatic potentials, and hence also the projected atom-column potentials, have finite width. In addition, electron scattering

at the column potentials introduces another pointspread. This pointspread of the scattered electron wave can be related to an "object resolution."

Both object resolution and instrumental resolution determine the structure resolution, which is the important value for practical work. Van Dyck et al. (1992, 2004; Van Dyck & de Jong, 1992) have already surveyed importance and relation of object resolution and instrumental resolution, but more than 10 years ago instrumental resolutions were distinctly worse than the estimates for object resolution: ∼0.1 nm for light atoms and ∼0.05 nm for heavy atoms.

Today instrumental resolutions have reached the range of these estimates, and it is therefore useful to calculate object resolution, instrumental resolution, and structure resolution numerically for objects of different scattering power and for an instrument with a very high resolution limit, adjusted for optimum contrast transfer.

Throughout this work we have chosen as a model structure an atom column comprising 5 atoms distributed evenly over a column length of $t = 2$ nm. The atom species was varied to be C, Si, and Ge, in order to investigate the effect of varying scattering power, and a Debye–Waller factor of 0.006 nm^2 has been applied to the hypothetical column structure, regardless of the atom species. A hypothetical instrument was chosen to have an accelerating voltage of 300 kV, an information limit of 0.05 nm, corresponding to a defocus spread of 1.13 nm, and a semi-convergence angle of the illumination of 0.2 mrad. The instrument was assumed to be adjusted for optimum negative phase contrast, with defocus $C_1 = 2.2$ nm, third-order spherical aberration $C_3 = -1.85$ μm, and fifth-order spherical aberration $C_5 = 0$ mm, according to the set of coefficients (3). A defocus correction of $t/2 = -1$ nm toward the column midplane was used for image simulation, according to (8). Electron scattering and nonlinear imaging under partially coherent illumination were calculated using the EMS simulation package (Stadelmann, 1987).

The widths, full width at half maximum (FWHM), of the modulations of the projected potential, of the scattered electron wave, and of the intensity at and near the column position were measured from respective line traces. Figures 5, 6, and 7 display these line traces, and the inset numbers denote the full peak widths at half maximum, which are compiled in Table 1. The width of the projected potential decreases from 0.045 nm for the C column, over 0.040 nm for the Si column, to 0.036 nm for the Ge column.

The width of the scattered electron wave decreases from 0.073 nm for the C column, over 0.065 nm for the Si column, to 0.048 nm for the Ge column; the widths are distinctly larger than the respective widths of the projected potentials. These observations are in accordance with the quantum-mechanical picture of high-energy electron channeling: below a certain scattering power the modulation of the scattered electron wave is related to the first bound state of the column potential. By quantum-mechanical principles

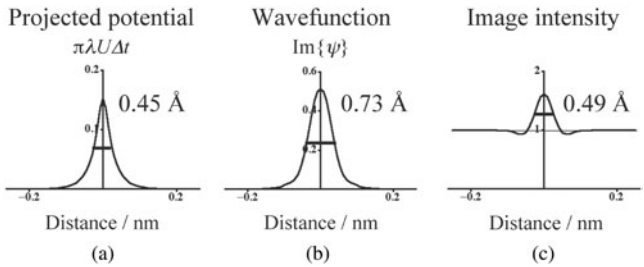

Figure 5. Contrast of a single column of C atoms for an accelerating voltage of 300 kV and an information limit of 0.5 Å. **a:** Projected potential of a specimen slice, thickness $\Delta t = 0.4$ nm, containing 1 C atom. **b:** Imaginary part of the exit wave function beneath a column, length 2 nm, comprising 5 C atoms. **c:** Image intensity of the 5-atom column at a lens defocus of +1.2 nm and a third-order spherical aberration of −1.85 μm. Inset numbers denote the full peak widths at half maximum.

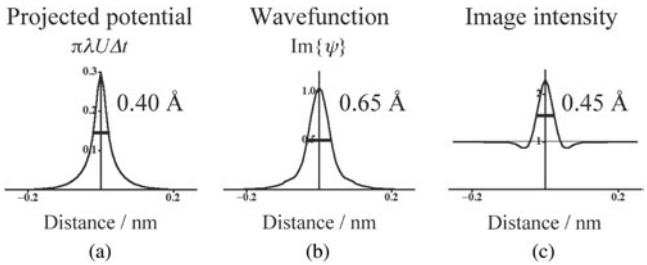

Figure 6. Contrast of a single column of Si atoms for an accelerating voltage of 300 kV and an information limit of 0.5 Å. **a:** Projected potential of a specimen slice, thickness $\Delta t = 0.4$ nm, containing 1 Si atom. **b:** Imaginary part of the exit wave function beneath a column, length 2 nm, comprising 5 Si atoms. **c:** Image intensity of the 5-atom column at a lens defocus of +1.2 nm and a third-order spherical aberration of −1.85 μm. Inset numbers denote the full peak widths at half maximum.

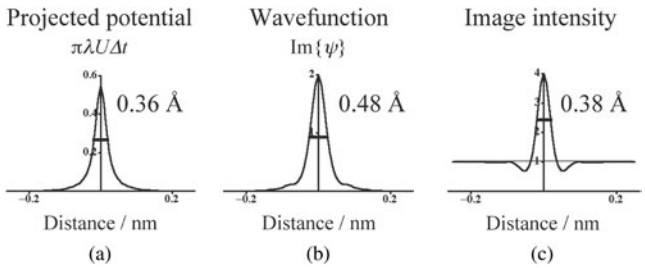

Figure 7. Contrast of a single column of Ge atoms for an accelerating voltage of 300 kV and an information limit of 0.5 Å. **a:** Projected potential of a specimen slice, thickness $\Delta t = 0.4$ nm, containing 1 Ge atom. **b:** Imaginary part of the exit wave function beneath a column, length 2 nm, comprising 5 Ge atoms. **c:** Image intensity of the 5-atom column at a lens defocus of +1.2 nm and a third-order spherical aberration of −1.85 μm. Inset numbers denote the full peak widths at half maximum.

Table 1. Full Peak Widths at Half Maximum of the Projected Potentials, the Imaginary Part of the Exit Waves, and the Image Intensities of C, Si, and Ge Columns, as well as the Smallest Resolved Intercolumn Distances of C, Si, and Ge Columns, Inferred from Image Intensity Traces.

Atom column	FWHM potential (Å)	FWHM exit wave, imaginary part (Å)	FWHM image intensity (Å)	Smallest resolved column distance (Å)
C	0.45	0.73	0.49	0.70
Si	0.40	0.65	0.45	0.64
Ge	0.36	0.48	0.38	0.59

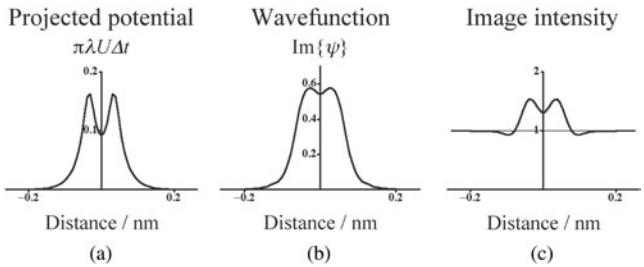

Figure 8. Contrast of two columns of C atoms for an accelerating voltage of 300 kV and an information limit of 0.5 Å. The intercolumn distance is 0.70 Å. **a:** Projected potential of a specimen slice containing 1 C atom per column. **b:** Imaginary part of the exit wave function beneath two columns, length 2 nm, each comprising 5 C atoms. **c:** Image intensity of the 5-atom columns at a lens defocus of +1.2 nm and a third-order spherical aberration of −1.85 μm.

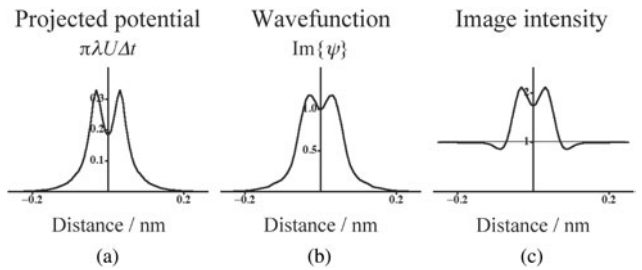

Figure 9. Contrast of two columns of Si atoms for an accelerating voltage of 300 kV and an information limit of 0.5 Å. The intercolumn distance is 0.64 Å. **a:** Projected potential of a specimen slice containing 1 Si atom per column. **b:** Imaginary part of the exit wave function beneath two columns, length 2 nm, each comprising 5 Si atoms. **c:** Image intensity of the 5-atom columns at a lens defocus of +1.2 nm and a third-order spherical aberration of −1.85 μm.

this bound state extends into the vacuum region close to the column, and the extension decreases for increasing column potential.

The contrast width of the intensity decreases from 0.049 nm for the C column, over 0.045 nm for the Si column, to 0.038 nm for the Ge column; the widths are distinctly smaller than the respective widths of the scattered electron waves. At first sight this result seems paradoxical, because the imperfect imaging of the scattered electron wave by the instrument, which transmits small spatial frequencies poorly and introduces a delocalization in the image plane, should broaden the column contrast further. The image intensity is, however, the modulus squared of the electron wave in the image plane, and the square of the contrast peak related to the atom column has a smaller width, roughly by $1/\sqrt{2}$, than the width of the contrast peak of the electron wave.

In the second part of this study, values for the structure resolution were derived from simulations for a model structure of two adjacent columns of the same type as described above and the same hypothetical instrument adjusted for optimum sub-angstrom contrast transfer. The intercolumn distance was varied until the value of the image intensity between the column locations dropped to a fraction of ∼0.81 of the peak values, similar to the Rayleigh resolution criterion. The atom species of the double-column structure was varied to be C, Si, and Ge, in order to investigate the effect of different scattering power.

Figures 8, 9, and 10 display the line traces for the modulation of the projected potential, of the scattered electron wave, and of the image intensity. The smallest, just-resolved intercolumn distance, at the level of the image intensity, decreases from 0.070 nm for the C column, over 0.064 nm for the Si column, to 0.059 nm for the Ge column (Table 1). From the line traces at the wave-function level, one can deduce that, for the small scattering power of C and the medium scattering power of Si, the double-column structure is not resolved; it is resolved for the strong scattering power of Ge. From the line traces of the projected potential, one can deduce that the double-column structure is well resolved in all cases.

Figure 11 compiles all measured values of the single-column and double-column simulation study in graphical form, and the following tendencies can be seen: (1) The width of the modulations of projected potential, wave function, and image intensity decreases for increasing scattering power, as well as the smallest resolved intercolumn distance; (2) the structure resolution inferred from the image intensity is not a fixed value for a given instrument; it improves for increasing scattering power, but it does not reach the instrumental information limit; (3) structure resolutions inferred from the projected potential are slightly better than structure resolutions inferred from the image intensity.

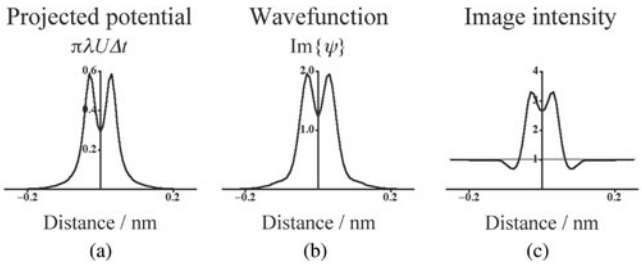

Figure 10. Contrast of two columns of Ge atoms for an accelerating voltage of 300 kV and an information limit of 0.5 Å. The intercolumn distance is 0.59 Å. **a:** Projected potential of a specimen slice containing 1 Ge atom per column. **b:** Imaginary part of the exit wave function beneath two columns, length 2 nm, each comprising 5 Ge atoms. **c:** Image intensity of the 5-atom columns at a lens defocus of +1.2 nm and a third-order spherical aberration of −1.85 μm.

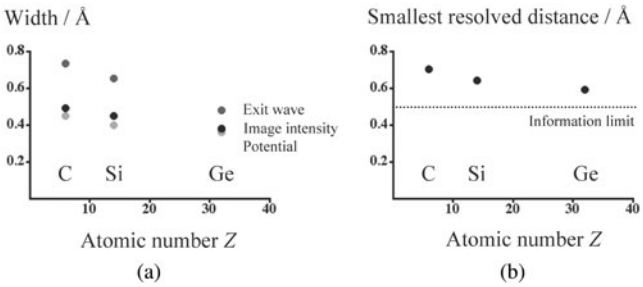

Figure 11. a: Full peak widths at half maximum of the projected potentials, the imaginary part of the exit waves, and the image intensities of C, Si, and Ge columns versus the atomic number of C, Si, and Ge. **b:** Smallest resolved intercolumn distances of C, Si, and Ge columns, inferred from image intensity traces, versus the atomic number of C, Si, and Ge.

Discussion

Optimum contrast transfer in the transmission electron microscope cannot, in principle, be given by a single objective criterion: first, a choice is made on which aspect of contrast transfer should be optimized; then, a mathematical criterion is chosen to calculate the set aberration coefficients determining the microscope adjustment. Aspects on contrast transfer comprise the amount of phase contrast, the delocalization in the image plane, the transfer of small spatial frequencies, the importance of high spatial frequencies, the number of contrast reversals, and so forth.

In this work we have chosen the amount of phase contrast to be most important. The mathematical way to determine the respective set of aberration coefficients, however, comprises a number of benefits for some of the other aspects as well.

First, the least-squares optimization of the aberration function (2) can be easily extended for higher order aberrations, such as seventh-order spherical aberration C_7, or any residual aberrations with noncircular symmetry, because it involves simple integration of powers of spatial frequencies g. This is an advantage over the treatments by Scherzer (1970) or Chang et al. (2006), where roots of higher order polynomials have to be calculated analytically, which is impossible to extend to noncircular symmetries.

Second, the optimization in two-dimensional space of spatial frequencies includes a stronger weighting of higher spatial frequencies, by the factor g in (2), than previous one-dimensional treatments. By this means the aberration function (1) maintains an optimum value of around $\pm\pi/2$ up to the information limit, and almost naturally the large gradient just before the zero of the contrast transfer function, which gives rise to larger delocalization, is avoided. In the treatment by Chang et al. (2006), for one set of aberration coefficients, their expressions B.10, B.11, and B.12, a zero of the contrast transfer function and a zero of the gradient of the aberration function are placed at the information limit. Their result is a different compromise between phase contrast and delocalization: the amount of phase contrast is distinctly smaller for higher spatial frequencies than for our set (4), at the benefit of smaller delocalization.

Third, both treatments, this and the one by Chang et al. (2006), have as a result a set of optimum aberration coefficients for the case of variable fifth-order spherical aberration C_5, which improve the transfer of lower spatial frequencies. It should be noted, however, that the lower bound of the Scherzer passband, $\sim$5 nm^{-1} for an accelerating voltage of 300 kV and a sub-angstrom information limit of 1/0.07 nm^{-1}, is still too large to transmit low-index crystal reflections, such as the {111} beams of Ge, properly. The result would be a severe imaging artifact, similar to the one observed by Tillmann et al. (2004) in an optimum negative phase-contrast image of GaAs, in the form of broad intensity maxima at tunnel positions of the [110] structure projection.

Structure resolution in sub-angstrom transmission electron microscopy, that is, the power to resolve, for example, two adjacent atom columns in crystalline material according to the Rayleigh criterion, has become dependent on both the instrumental pointspread function and the resolution limit given by the object. For resolutions distinctly larger than 1 Å, structure resolution was given essentially by the pointspread function of the instrument, because the effect of finite object resolution was much smaller. Now, at the sub-angstrom scale, information limits are approaching the values for object resolutions, which are dependent on the scattering power of the object. Therefore no sharp value for structure resolution can be given; instead numerical simulations have to be carried out in order to assess the product of the two convolutions given by the respective instrumental pointspread and the object pointspread. In this study, structure resolutions were found to range from

0.070 nm for a weakly scattering C column down to 0.059 nm for a more strongly scattering Ge column, despite an instrumental information limit as good as 0.050 nm.

The mere recording of one image under "optimum" conditions may not be sufficient to obtain a faithful image of the object under investigation. The optimum structure image will be degraded in practice by the following circumstances: (1) It is very difficult to adjust the instrument precisely for the desired aberrations and to keep the optimum adjustment long enough to record the desired optimum images; (2) large fixed aberrations, such as sixfold astigmatism A_5, which may be as large as the fifth-order spherical aberration C_5, can degrade the instrumental resolution through delocalization; (3) the unavoidable weak transfer of small spatial frequencies adds strong imaging artifacts, as described above.

Wave function reconstruction (Lichte, 1986; Coene et al., 1992; Thust et al., 1996) can be used to remove the above imaging artifacts *a posteriori*. On the one hand, one can see from the simulation study that the width of the contrast modulation is larger on the wave function level, compared to the image level; that is, the related structure resolution on the wave function level is worse than that on the image level. On the other hand, the imaging artifacts may be too large in practice to exploit the extra resolution offered on the image level at all. In addition, the very small defocus levels to be applied in optimum imaging can be easily missed, in particular the minute values for the sub-angstrom scale, and therefore the recording of through-focus series of images, which may be exploited for wave function reconstruction, will be an important means for sub-angstrom structure imaging.

Conclusions

In sub-angstrom transmission electron microscopy, aberrations of the imaging system of at least the fifth order play a role for high-resolution structure imaging.

Two sets of aberration coefficients are derived for optimum phase contrast from a thin specimen: one for variable lens defocus C_1, variable third-order spherical aberration C_3, and fixed fifth-order spherical aberration C_5, and another for variable lens defocus C_1, variable third-order spherical aberration C_3, and variable fifth-order spherical aberration C_5. Both positive and negative phase contrast can be achieved by choosing the proper sign of the coefficients.

For the derivation of the optimum aberration coefficients, a least-squares fit has been used, which applies to the two-dimensional lens aberration function over the virtual aperture given by the temporal coherence envelope. The two-dimensional treatment of the optimization problem leads to an advantageous stronger weighting of higher spatial frequencies, which provides not only optimum phase contrast up to the information limit of the instrument but also only moderate delocalization in the image plane.

For information limits at the sub-angstrom scale, the optimum lens defocus C_1 may reach values of a few nanometers, which is the same scale as the thickness of the objects used in high-resolution imaging. Therefore the proper placement of the reference plane for numerical image simulations, the Gaussian image plane, becomes important. In standard image simulation programs the reference plane is placed at the exit face of the model object, but for the interpretation of structure images, placement at the midplane of the object is favorable. Then the optimum lens defoci C_1 have to be corrected by an underfocus equal to half the object thickness for image simulation studies.

The resolution under optimum contrast transfer is still strongly determined by the combined effect of the instrumental information limit and the residual delocalization in the image plane, which determine the instrumental pointspread. At the sub-angstrom scale, however, also the finite width of the modulation of the scattered electron wave becomes important, which determines an "object resolution."

The "structure resolution," that is, the power to resolve, for example, two adjacent atom columns of a crystalline object in a high-resolution image, is determined by both instrumental pointspread and object resolution. For instruments with sub-angstrom information limits, both contributions have similar weight, and the simulation study in this work revealed values ranging from 0.070 nm for weakly scattering columns down to 0.059 nm for stronger scattering columns, which were still distinctly larger than the assumed instrumental information limit of 0.050 nm.

The simulation study revealed further that structure resolutions deduced from a high-resolution image may be significantly better than structure resolutions deduced from the appertaining scattered electron wave. In practice, however, structure resolutions will be degraded by the difficulty of aligning the instrument precisely, which introduces additional delocalization in the image plane, and most strongly by imaging artifacts introduced through the weak contrast transfer at small spatial frequencies.

Addendum

If the influence of the seventh-order spherical aberration C_7 becomes important for high-resolution imaging, then the aberration function (1) extends by a term $\frac{1}{8}C_7\lambda^7(g_1^2+g_2^2)^4$, and the optimum set of aberrations (4) is modified by corrections proportional to C_7 according to

$$C_1 = \frac{15}{4\lambda g_{\max}^2} - \frac{5C_7\lambda^6 g_{\max}^6}{112}, \tag{9a}$$

$$C_3 = -\frac{15}{\lambda^3 g_{\max}^4} + \frac{15 C_7 \lambda^4 g_{\max}^4}{28}, \tag{9b}$$

$$C_5 = \frac{105}{8\lambda^5 g_{\max}^6} - \frac{45 C_7 \lambda^2 g_{\max}^2}{32}. \tag{9c}$$

Defocus C_1, third-order spherical aberration C_3, and fifth-order spherical aberration C_5 are assumed to be variable, and C_7 is assumed to be fixed.

Acknowledgments

The author thanks H. Rose, Darmstadt, M. Haider, Heidelberg, and colleagues A. Thust, L. Houben, and K. Urban at Jülich for the many inspiring discussions on electron optics, aberration correction, wave function reconstruction, and practical aspects of high-resolution microscopy, and for support during the past years.

References

Benner, G., Matijevic, M., Orchowski, A., Schindler, B., Haider, M. & Hartel, P. (2003). State of the first aberration-corrected, monochromized 200 kV FEG-TEM. *Microsc Microanal* **9**(Suppl. 2), 938–939.

Bethe, H. (1928). Theorie der Beugung von Elektronen an Kristallen. *Annalen der Physik* **87**, 55–129.

Bonhomme, P. & Beorchia, A. (1983). The specimen thickness effect upon electron microscope image contrast transfer of amorphous objects. *J Phys D Appl Phys* **16**, 705–713.

Chang, L.Y., Kirkland, A.I. & Titchmarsh, J.M. (2006). On the importance of fifth-order spherical aberration for a fully corrected electron microscope. *Ultramicroscopy* **106**, 301–306.

Coene, W. & Jansen, A.J.E.M. (1992). Image delocalisation and high resolution transmission electron microscopic imaging with a field emission gun. *Scan Microsc* **6**(Suppl.), 379–403.

Coene, W., Janssen, G., Op de Beeck, M. & Van Dyck, D. (1992). Phase retrieval through focus variation for ultra-resolution in field-emission transmission electron microscopy. *Phys Rev Lett* **69**, 3743–3746.

Cowley, J.M. & Moodie, A.F. (1957). The scattering of electrons by atoms and crystals. I. A new theoretical approach. *Acta Cryst* **10**, 609–619.

Freitag, B., Kujawa, S., Mul, P.M., Ringnalda, J. & Tiemeijer, P.C. (2005). Breaking the spherical and chromatic aberration barrier in transmission electron microscopy. *Ultramicroscopy* **102**, 209–214.

Fujimoto, F. (1978). Periodicity of crystal structure images in electron microscopy with crystal thickness. *Phys Status Solidi A* **45**, 99–106.

Haider, M., Uhlemann, S., Schwan, E., Rose, H., Kabius, B. & Urban, K. (1998). Electron microscopy image enhanced. *Nature* **392**, 768–769.

Jia, C.L., Lentzen, M. & Urban, K. (2003). Atomic-resolution imaging of oxygen in perovskite ceramics. *Science* **299**, 870–873.

Jia, C.L., Lentzen, M. & Urban, K. (2004). High-resolution transmission electron microscopy using negative spherical aberration. *Microsc Microanal* **10**, 174–184.

Jia, C.L. & Urban, K. (2004). Atomic-resolution measurement of oxygen concentration in oxide materials. *Science* **303**, 2001–2004.

Kambe, K., Lehmpfuhl, G. & Fujimoto, G. (1974). Interpretation of electron channeling by the dynamical theory of electron diffraction. *Z Naturforsch A* **29**, 1034–1044.

Kisielowski, C., Hetherington, C.J.D., Wang, Y.C., Kilaas, R., O'Keefe, M.A. & Thust, A. (2001). Imaging columns of the light elements carbon, nitrogen and oxygen with sub Ångstrom resolution. *Ultramicroscopy* **89**, 243–263.

Lentzen, M. (2004). The tuning of a Zernike phase plate with defocus and variable spherical aberration and its use in HRTEM imaging. *Ultramicroscopy* **99**, 211–220.

Lentzen, M., Jahnen, B., Jia, C.L., Thust, A., Tillmann, K. & Urban, K. (2002). High-resolution imaging with an aberration–corrected transmission electron microscope. *Ultramicroscopy* **92**, 233–242.

Lichte, H. (1986). Electron holography approaching atomic resolution. *Ultramicroscopy* **20**, 293–304.

Lichte, H. (1991). Optimum focus for taking holograms. *Ultramicroscopy* **38**, 13–22.

O'Keefe, M.A. (2000). The optimum C_S condition for high-resolution transmission electron microscopy. *Microsc Microanal* **6**, 1036–1037.

O'Keefe, M.A., Allard, L.F. & Blom, D.A. (2005). HRTEM imaging of atoms at sub-Ångström resolution. *J Electron Microsc* **54**, 169–180.

O'Keefe, M.A., Dahmen, U. & Hetherington, C.J.D. (1989). Simulated image maps for use in experimental high-resolution electron microscopy. *Mat Res Soc Sym Proc* **159**, 453–458.

O'Keefe, M.A., Hetherington, C.J.D., Wang, Y.C., Nelson, E.C., Turner, J.H., Kisielowski, C., Malm, J.-O., Mueller, R., Ringnalda, J., Pan, M. & Thust, A. (2001). Sub-ångstrom high-resolution transmission electron microscopy at 300 kV. *Ultramicroscopy* **89**, 215–241.

O'Keefe, M.A. & Kilaas, R. (1988). Advances in high-resolution image simulation. *Scan Microsc* **2**(Suppl.), 225–244.

Rose, H. (1989). Bildenstehung im Elektronenmikroskop. Lecture at Technical University Darmstadt, 183 pages.

Rose, H. (1990). Outline of a spherically corrected semiaplanatic medium-voltage transmission electron microscope. *Optik* **85**, 19–24.

Scherzer, O. (1949). The theoretical resolution limit of the electron microscope. *J Appl Phys* **20**, 20–29.

Scherzer, O. (1970). Die Strahlenschädigung der Objekte als Grenze für die hochauflösende Elektronenmikroskopie. *Berichte der Bunsengesellschaft* **74**, 1154–1167.

Scherzer, O. & Typke, D. (1967). Die Auflösungsgrenze eines in zwei Schnitten sphärisch korrigierten Objektivs. *Optik* **26**, 564–573.

Smith, D.J., Saxton, W.O., O'Keefe, M.A., Wood, G.J. & Stobbs, W.M. (1983). The importance of beam alignment and crystal tilt in high resolution electron microscopy. *Ultramicroscopy* **11**, 263–281.

Stadelmann, P.A. (1987). EMS—A software package for electron diffraction analysis and HREM image simulation in materials science. *Ultramicroscopy* **21**, 131–145.

Thust, A., Coene, W.M.J., Op de Beeck, M. & Van Dyck, D. (1996). Focal-series reconstruction in HRTEM: Simulation studies on non-periodic objects. *Ultramicroscopy* **64**, 211–230.

Tillmann, K., Thust, A. & Urban, K. (2004). Spherical aberration correction in tandem with exit-plane wave function reconstruction: Interlocking tools for the atomic scale imaging of lattice defects in GaAs. *Microsc Microanal* **10**, 185–198.

Van Dyck, D. & de Jong, A.F. (1992). Ultimate resolution and information in electron microscopy: General principles. *Ultramicroscopy* **47**, 266–281.

Van Dyck, D., Op de Beeck, M. & Coene, W. (1992). Information in electron microscopy. In *Image Interpretation and Image Processing in Electron Microscopy*, Heydenreich, J. & Neumann, W. (Eds.), pp. 6–31. Halle/Saale, Germany: Max Planck Institute for Microstructure Physics.

Van Dyck, D., Van Aert, S. & den Dekker, A.J. (2004). Physical limits on atomic resolution. *Microsc Microanal* **10**, 153–157.

Zernike, F. (1942*a*). Phase contrast, a new method for the microscopic observation of transparent objects, Part I. *Physica* **9**, 686–698.

Zernike, F. (1942*b*). Phase contrast, a new method for the microscopic observation of transparent objects, Part II. *Physica* **9**, 974–986.

Zernike, F. (1955). How I discovered phase contrast. *Science* **121**, 345–349.